INFLUENCE OF GRAIN SIZE ON α'Cr PRECIPITATION IN AN ISOTHERMALLY AGED Fe-21Cr-5Al ALLOY

Maalavan Arivu¹, Andrew Hoffman², Jonathan Poplawsky^{3,*}, Ian Spinelli², Cong Dai⁴, Raul B. Rebak², James Cole⁵, Rinat K. Islamgaliev⁶, Ruslan Z. Valiev^{6, 7}, Haiming Wen^{1,8,*}

¹Department of Materials Science and Engineering, Missouri University of Science and Technology, Rolla, MO 65409, USA

²General Electric Research, Schenectady, NY 12309, USA

³Oak Ridge National Laboratory, Oak Ridge, TN 37830, USA

⁴Canadian Nuclear Laboratories, Chalk River, ON K0J 1J0, Canada

⁵Idaho National Laboratory, Idaho Falls, Idaho 83415, USA

⁶Institute of Physics of Advanced Materials, Ufa State Aviation Technical University, Ufa 450008, Russia

⁷Saint Petersburg State University, St Petersburg, Russia, 199034

⁸Department of Nuclear Engineering and Radiation Science, Missouri University of Science and Technology, Rolla, MO 65409, USA

*Corresponding authors: wenha@mst.edu; poplawskyjd@ornl.gov

ABSTRACT

Cr-rich α'precipitation during aging typically leads to hardening and accordingly embrittlement of FeCrAl alloys, which needs to be suppressed. The influence of grain size on α'precipitation was studied by aging coarse-grained (CG), ultra-fine grained (UFG), and nanocrystalline (NC) ferritic Kanthal-D [KD; Fe-21Cr-5Al (wt.%) alloy] at 450, 500 and 550 °C for 500h. After aging at 450 and 500 °C, less hardening was observed in the UFG KD than in CG KD. Atom probe tomography indicated a lower

number density and larger sized intragranular α' in the UFG versus the CG alloy. The smaller grain size and higher defect (vacancy and dislocation) density in the UFG KD facilitated diffusion and accordingly enhanced precipitation kinetics, leading to coarsening of precipitates, as well as saturation of precipitation at lower temperatures, as compared to those in CG KD. No hardening occurred in UFG and CG KD after aging at 550 °C, indicating that the miscibility gap is between 500 and 550 °C. NC KD exhibited softening after aging owing to grain growth. α'precipitation occurred in NC KD aged at 450 °C but not at 500 °C, indicating that miscibility gap is between 450 and 500 °C. Thus, the significantly smaller grain size in NC KD decreased the miscibility gap, as compared to that in CG and UFG KD. This is attributed to the absorption of vacancies by migrating grain boundaries during aging, suppressing α' nucleation and enhancing Cr solubility.

1. INTRODUCTION

High Cr (>11 wt.%) ferritic Fe-Cr-Al alloys are a class of alloys that are sought after to replace Zr-based alloys as accident tolerant fuel cladding in light-water reactors (LWRs) owing to their superior oxidation resistance in high-temperature steam conditions [1–7]. However, due to the high Cr content in FeCrAl alloys, after aging at temperatures below the α - α ' miscibility gap, Cr-rich α ' precipitation occurs, leading to hardening and embrittlement of the alloys [8–11]. Several studies examined effects of Cr on the miscibility gap, which found that an increase in Cr content results in an increase in phase instability and a higher degree of α ' phase separation from the Fe-enriched α matrix [12–14]. The precipitation of Cr-enriched α ' phase is enabled by vacancy diffusion and

vacancy clusters serve as nucleation sites. Recent study by Jarmila et. al using positron annihilation spectroscopy complemented with Mössbauer spectroscopy confirms the binding of Cr atoms with vacancies and vacancy clusters in aged PM 2000TM [oxide dispersion strengthened (ODS) Fe-20Cr-5Al wt.%] [15].

Al stabilizes the FeCrAl solid solution and has been reported to suppress α' thermodynamically by lowering the miscibility gap. The atom probe tomography study by Capdevila et. al indicated the partitioning of Al away from the α' phase in PM2000 [16]. Read et. al also showed using atom probe field ion microscopy that Al separated from the Cr-enriched α' precipitates in MA 956 (Fe20Cr4.5Al ODS alloy) after long term aging at 475 °C [17]. Although Al represses the miscibility gap, Al has been shown to lower the formation enthalpy of vacancies, thereby increasing the thermal vacancy concentration in the matrix [18]. The higher the thermal vacancy concentration is, the higher the number of nucleation sites for α' is, and the faster the precipitation kinetics is. These studies confirm that the thermal vacancy concentration in the matrix plays an important role in α' precipitation.

If the thermal vacancy concentration can be decreased in high Cr ferritic FeCrAl alloys, precipitation/phase separation of α' can be reduced. This may be achieved by introducing a high density of vacancy sinks in the matrix. Grain boundaries (GBs) have been shown to be effective sinks for vacancies. Although GBs can act as sinks, they also can act as a vacancy source when the matrix vacancy concentration is below equilibrium [19]. Based on this consideration, in an FeCrAl alloy with a significant volume fraction of GBs or correspondingly a very small grain size, α' precipitation may be reduced due to

decreased thermal vacancy concentration. It is very important to investigate this aspect to improve the development of FeCrAl alloys with enhanced phase stability.

In order to study the effect of grain size on α' precipitation, Kanthal-D [KD, Fe-21Cr-5Al-0.026C wt.%], a commercial high-Cr ferritic FeCrAl alloy, was subjected to nanostructuring using two severe plastic deformation (SPD) techniques of equal-channel angular pressing (ECAP) and high-pressure torsion (HPT). The ECAP and HPT processed nanostructured variants, along with their coarse-grained counterpart, were aged at three temperatures of 450, 500 and 550 °C for 500h. The microstructure produced from ECAP of KD is very different from that of HPT KD [20]. After ECAP, KD exhibited a non-homogeneous microstructure with a multi-modal grain size distribution. However, there were two dominant grain size regimes, fine-grained [FG, average grain size (AGS) 1 -10 μm with large area fraction of low-angle GBs (LAGBs, misorientation 2° – 15°)] and ultra-fine grained (UFG, AGS 100 nm – 1 µm). HPT resulted in a homogeneous equiaxed microstructure with nanocrystalline (NC, AGS < 100nm) grains. The area fraction of high-angle GBs (HAGBs, misorientation >15°) is ~80% in HPT as opposed to ~49% in ECAP KD. Comparing the precipitation characteristics after aging of conventional coarse-grained (CG, AGS > 10 μm), ECAP produced UFG [UFG regions identified using electron back scatter diffraction (EBSD)], and HPT processed NC KD can establish an understanding of the influence of grain size on α' precipitation in FeCrAl alloys.

There exists only one study, which was carried out by Read and Murakami back in 1996 comparing the α' precipitation behavior after aging at 475 °C for 588h in extruded and rolled MA956 [ODS Fe-20Cr-4.5Al-0.5Ti-0.5Y₂O₃ (all in wt.%)] to that in

the recrystallized counterpart [21]. It was concluded that thermodynamic considerations for CG bulk materials may not be applicable to NC materials. However, MA956 is an ODS FeCrAl, where the precipitation characteristics is affected by the presence of dispersoids [22]. Our present work is the first to systematically study the impact of grain size on α' precipitation characteristics in a dispersoid free Fe-Cr-Al alloy matrix.

2. EXPERIMENTAL PROCEDURES

Cylindrical KD commercial bar stock (composition provided in Table 1) was subjected to solution treatment at 1050 °C for 1 h, followed by oil quenching and tempering at 800 °C for 1 h, before air cooling down to room temperature (here after referred to as 'CG KD').

Table 1. Elemental composition of KD.

Element	Fe	Cr	Al	Ni	Si	Mn	Zr	V	C	Ti,
										Co
At.%	Bal.	20.66	9.27	0.26	0.45	0.17	0.09	0.03	0.11	0.02

ECAP KD was carried out on heat treated KD bar stock at a temperature of 520 $^{\circ}$ C up to six passes following the B_c route [23]. The inner contact angle between the channels of the ECAP die was 120°. Heat treated KD bar stock was sectioned to ~2 mm thick discs, and HPT was performed on the discs under a pressure of 6 GPa at 300 °C for ten rotations, at 0.2 rotations per minute [24]. The final thickness of the discs after HPT

was measured to be \sim 1.2 mm. Aging was performed in an alumina tube furnace under an Ar atmosphere at a heating rate of 10 °C/ min to attain the desired temperatures of 450, 500 or 500 °C, with a holding time of 500h. A thermocouple was used to ensure that the temperature fluctuation remained within \pm 2 °C. After aging, the samples were air cooled down to room temperature. Vickers microhardness was obtained after aging using a Struers Duramin5 Vickers hardness tester by applying a force of 4.91 N for 5 s.

Back scatter (BSE) scanning electron microscopy (SEM) of aged HPT KD was performed using a FEI Helios NanoLab 600 scanning electron microscope. A trench of 50 nm depth was made on the surface of aged HPT KD using a focused ion beam (FIB) in the same SEM to increase the contrast between the grains. EBSD of aged ECAP KD using an Oxford HKL EBSD system in the same SEM was carried out to quantify GB character and grain size. Samples for EBSD were prepared by mechanical polishing using down to 0.02 µm colloidal silica for 45 min. APT specimens were fabricated using standard lift-out and sharpening methods as described by Thompson et al. using a Thermo Fisher Nova 200 Dual Beam scanning electron microscope/focused ion beam (SEM/FIB) [25]. UFG regions in ECAP KD were identified using EBSD and marked using Pt deposition. Focused ion-beam lift-outs to prepare APT specimens of ECAP KD were carried out in the Pt marked regions. Herein, any reference to precipitation in ECAP KD only applies to the UFG regions in it. The reason why samples are not named after their initial grain size post thermo-mechanical processing (ECAP or HPT) is that microstructural changes (e.g., grain growth) occur when subjected to thermal aging. Thus, the samples are labelled using the thermo-mechanical processing (ECAP or HPT) they underwent. The APT experiments were run using a CAMECA LEAP 4000XHR in

voltage mode with a 50K base temperature, 20% pulse fraction, and a 0.5% detection rate. The APT results were reconstructed and analyzed using CAMECA's interactive visualization and analysis software (IVAS 3.8). The most straightforward method of representing experimental data for the purpose of illuminating interfacial segregation or phase separation is through the use of the proximity histogram, often known as the "proxigram," which is a profile of local atomic concentrations vs. vicinity to an interface [26]. Thus, proxigrams can be used to identify phase separation. However, proxigram method cannot be used to accurately determine the chemical composition of the separated phase when the precipitates are extremely small and have complex shapes. In addition, when a single statistical proxigram is computed based on an average interface for all precipitates in the system, that is, when all of the individual proxigrams for every particle of varying size and complex geometry are added together, which is commonly used, an artificially widened interface will be produced [27]. This is merely an effect associated with computing concentration profiles across particles of different sizes and shapes, however, it could be incorrectly understood as an intermixing between the precipitates and the matrix [28–30]. Therefore, Cr and Ni iso-concentration surfaces and the proxigrams based on them are only used to visualize and identify α' and Al-Ni precipitates, respectively. It is not the intended purpose of this work to accurately measure the composition of the α ' and Al-Ni precipitates. Details of cluster analysis used to quantify α' phase separation has been provided in the discussion section.

3. RESULTS

3.1. Hardness changes in CG, ECAP AND HPT KD after aging

Vickers microhardness was measured on CG, ECAP, and HPT KD, before aging and after aging at 450 °C and 500 °C for 500h as shown in Figure 1. Unaged CG and ECAP KD have a hardness of 228 ± 2 HV and 333 ± 10 HV, respectively. The hardness of CG and ECAP KD after aging at 450 °C was found to be 333 ± 6 HV and 408 ± 5 HV, respectively. After aging at 500 °C for 500h, a hardness of 380 ± 9 HV and 414 ± 4 HV was measured for CG and ECAP KD, respectively. Comparing the unaged and the aged specimens, after aging at 450 °C CG KD exhibited a hardening of ~105 HV (46%), and ECAP KD had a hardness increase of ~75 HV (22.5%). After aging at 500 °C, ECAP KD only shows a minimal hardness increase of ~6 HV (1.8%) in comparison to ECAP KD aged at 450 °C. However, a hardness increase of ~47 HV (14%) is found in CG KD after aging at 500 °C as compared to CG KD aged at 450 °C. While both CG and ECAP KD show hardening, HPT KD exhibits softening after aging at 450 °C and 500 °C. Due to this difference, CG and ECAP KD were studied together, and separately from HPT KD.

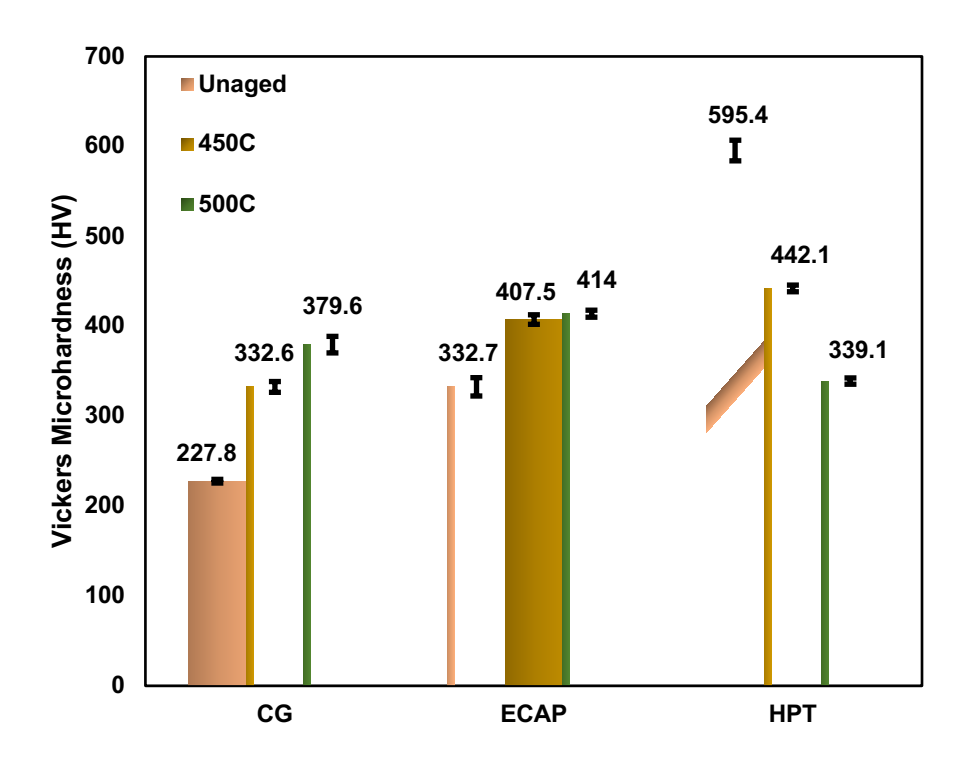


Figure 1. Average Vickers microhardness obtained from CG, ECAP and HPT KD, unaged and aged at 450 and 500 °C for 500h.

3.2. Comparison in microstructure between aged CG and aged ECAP KD

Iso-concentration surface analysis in APT reveals the Cr-enriched α' phase separation in CG KD aged at 450 and 500 °C, as can be seen in Figure 2a and 2b. This separation caused hardening in CG KD after aging at both temperatures. The concentration of Cr in the α' was measured to be ~60-65 at.% from proximity histograms (proxigrams) displayed in Figure 2c) based on 35 at.% Cr iso-concentration surfaces of the 450 °C aged CG KD. As compared to 450 °C aged CG KD, 500 °C aged CG KD exhibits a higher Cr concentration of ~70-75 at.%, as evident in Figure 2d. Cr and Si were found to be enriched, and Fe and Al were found to be depleted in the α' phase separated out in both 450 °C and 500 °C aged CG KD.

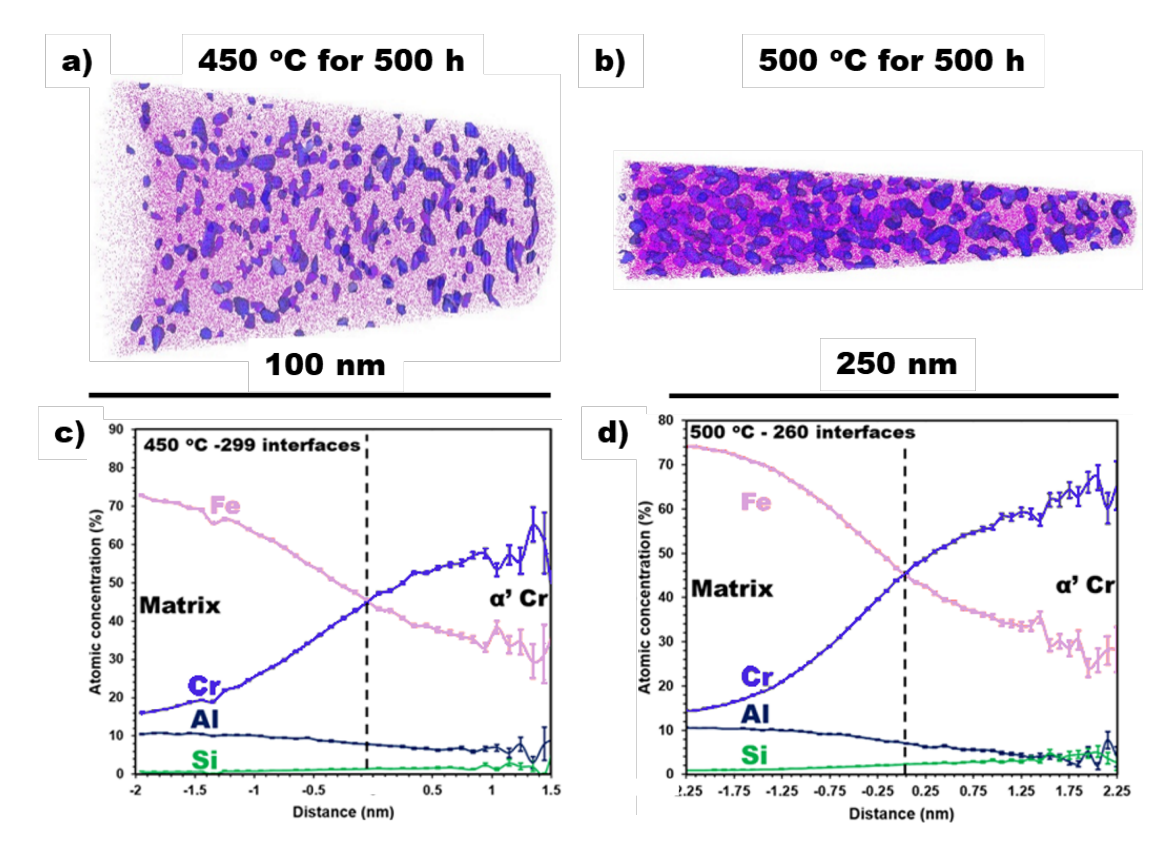


Figure 2. APT reconstruction of a) 450 °C, and b) 500°C aged CG KD, where Fe atoms (pink) and 35 at.% Cr iso-surface (blue) are displayed; proxigrams based on 35 at.% Cr iso-surfaces from c) 450 °C, and d) 500 °C aged CG KD.

Due to the high defect density introduced in an alloy during SPD (even at elevated temperatures), there is a possibility of enhanced precipitation during the process [20]. Therefore, unaged ECAP KD was studied using APT to check for the possible presence of α' precipitates. As can be seen from Figure 3a, the α' phase was not found in unaged ECAP KD, and it can thus be concluded that ECAP processing at 520 °C did not lead to α' precipitation in KD. Precipitation of α' was found in aged ECAP KD, which is ascribed as the reason for the hardening on aging in ECAP KD (Figure 3b and 3c). From the proxigrams shown in Figure 3d and 3e, Cr and Si were enriched, whereas Fe and Al were depleted in the α' phase. The Cr concentration in the α' phase is lower in the 450 °C aged

ECAP KD in comparison to that in the 500 °C aged ECAP KD, similar to what was observed in aged CG KD.

CG KD is thermally stable during long term aging at 450 and 500 °C, as the average grain size is in the range of hundreds of microns[20]. In contrast, due to the high dislocation density and the significant volume fraction of GBs after SPD, the microstructure of ECAP KD may become thermally unstable [20,31,32]. Therefore, it is important to scrutinize the microstructure of ECAP KD after aging at both temperatures. It can be observed from Figure 4a and 4b that the microstructure of ECAP KD aged at 450 °C and 500 °C resembles that of unaged ECAP KD presented elsewhere [20]. 450 °C and 500 °C aged ECAP KD exhibited a fraction of LAGBs of 72% and 57%, respectively; the high fraction of LAGBs is a typical microstructural characteristic of ECAP processed alloys. Although the fraction of LAGBs decreased with increasing aging temperature, there was no sign of significant recrystallization or grain growth as observed in a previous study on thermal stability [32]. This confirms that ECAP KD is thermally stable during isothermal aging and that the hardening observed in ECAP KD after aging corresponds to α' precipitation. Thus, age hardening is expected to be mainly due to α' precipitation in both CG and ECAP KD.

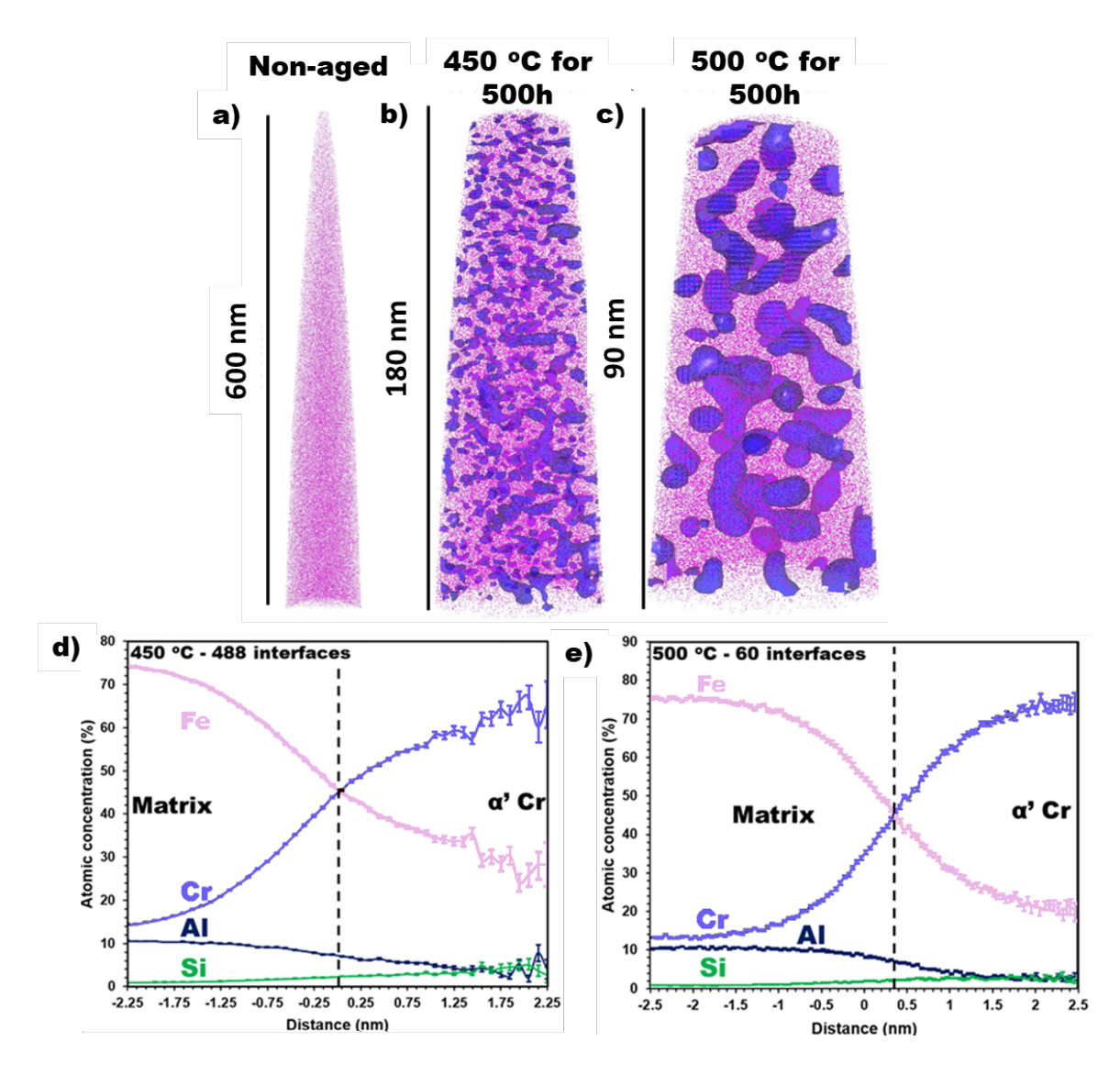


Figure 3. APT reconstruction of a) unaged, b) 450 °C, and c) 500 °C aged ECAP KD, where Fe atoms (pink) and 35 at.% Cr iso-surfaces (blue) are displayed; proxigrams based on 35 at.% Cr iso-surfaces from d) 450 °C, and e) 500 °C aged ECAP KD.

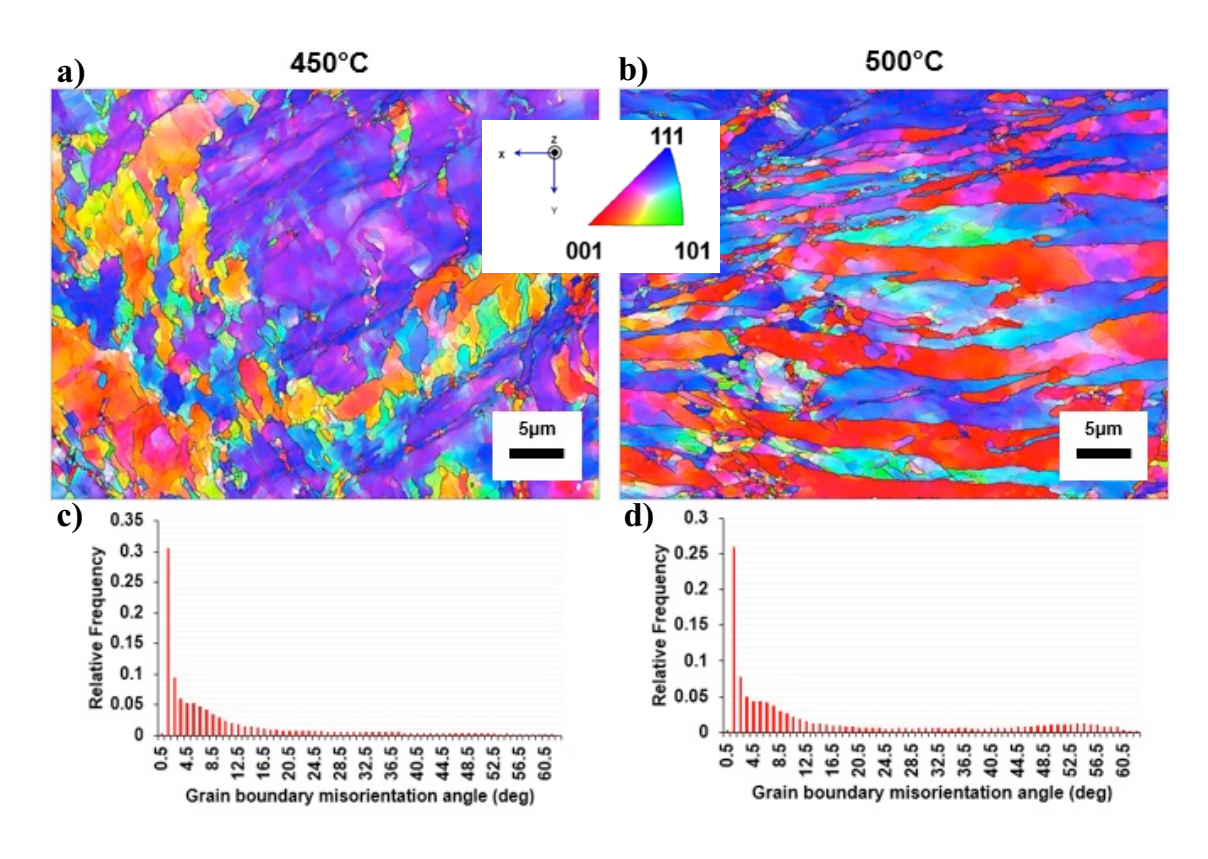


Figure 4. Inverse pole figure orientation map obtained from EBSD showing LAGBs (red) and HAGBs (black) in a) ECAP KD aged at 450 °C, and b) ECAP KD aged at 500 °C. GB misorientation angle distribution in c) ECAP KD aged at 450 °C, and d) ECAP KD aged at 500 °C.

Al-Ni precipitation was identified in both CG and ECAP KD aged at 450 °C and 500 °C, as shown in Figure 5a-d. The proxigram based on 2 at.% Ni iso-concentration surface in Figure 5e indicates the enrichment of Al and Ni suggesting Al-Ni precipitation. In contrast, Fe and Cr were depleted. The interparticle distance between Al-Ni precipitates is high and the number density is very low, and therefore, these precipitates wouldn't play a big role in hardening. However, it is interesting to note the nanoscale precipitation of this secondary phase along with α' during isothermal aging. These precipitates were not found in CG and ECAP KD prior to aging.

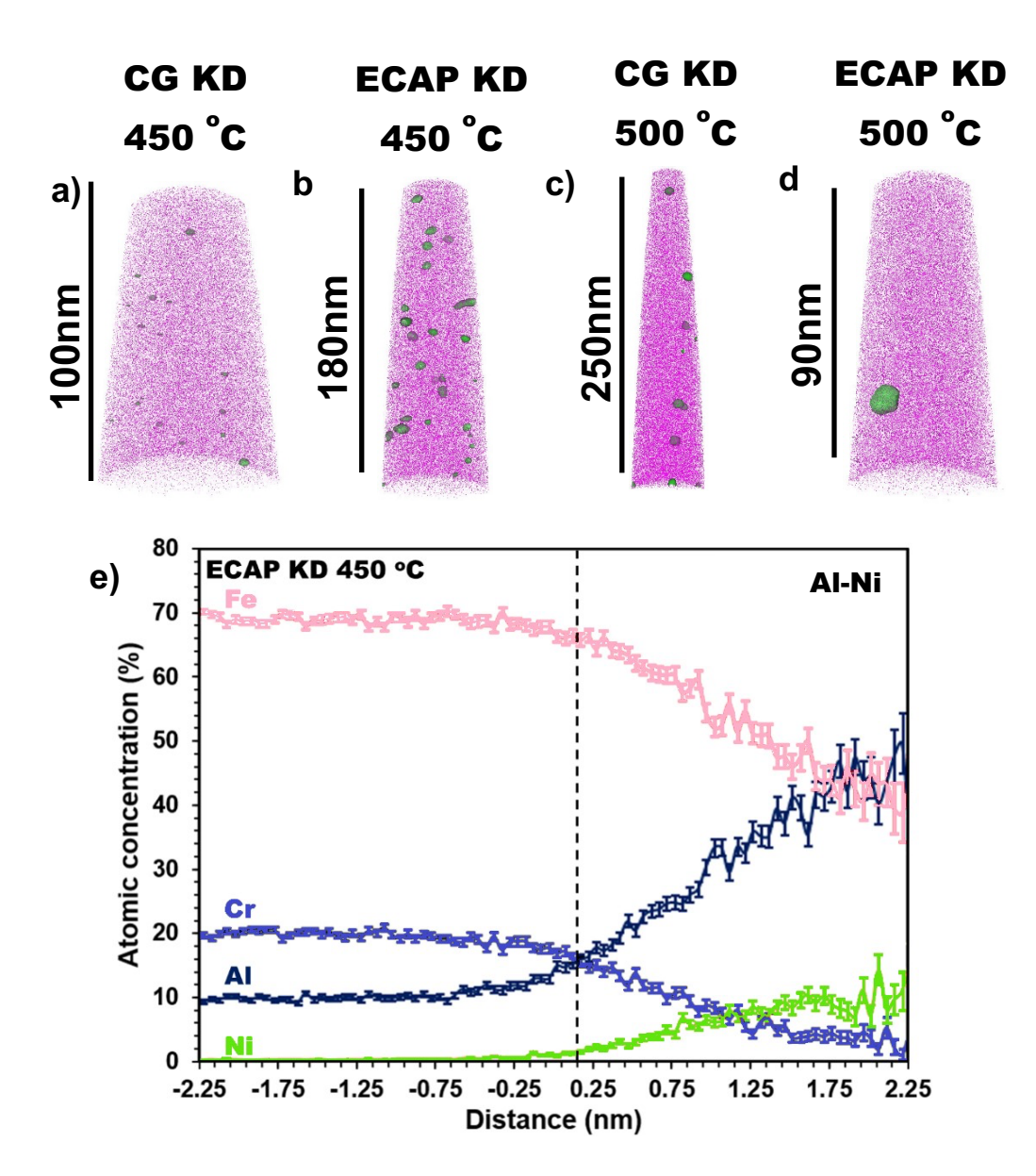


Figure 5. APT reconstruction of a) CG KD aged at 450 °C, b) ECAP KD aged at 450 °C, c) 500C °C aged CG KD, and d) 500C °C aged ECAP KD, where Fe atoms (pink) and 2 at.% Ni iso-surfaces (green) are displayed; e) proxigrams based on 2 at.% Ni iso-surface from ECAP KD aged at 450 °C for 500h.

3.3. Microstructure of aged HPT KD

Figure 6a and 6b show the APT reconstruction of HPT KD isothermally aged at 450 °C and 500 °C for 500h, respectively. While 35 at.% Cr iso-surfaces (blue) reveal the

precipitation of α' at 450 °C, no α' precipitation is found in HPT KD aged at 500 °C. The α' phase in HPT KD aged at 450 °C is enriched with Cr and Si and is depleted of Fe and Al. The Cr concentration is ~65%, consistent with that in the α' phase in aged CG and ECAP KD. While α' phase separation was identified in HPT KD aged at 450 °C, no orthorhombic Al₃Ni precipitation was observed in HPT KD aged at 450 °C or 500 °C from APT.

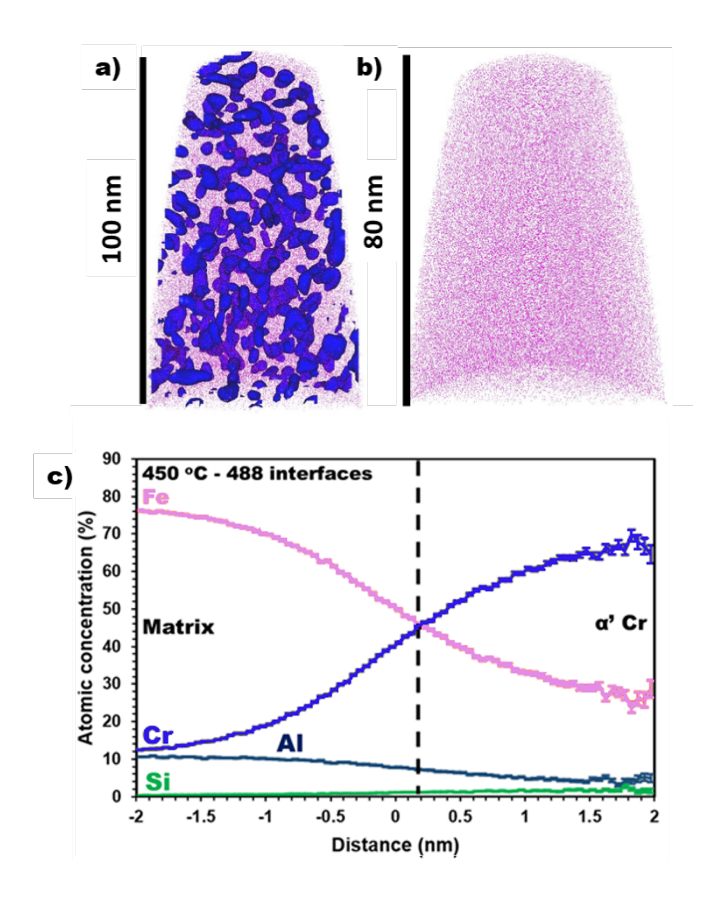


Figure 6. APT reconstruction of a) HPT KD aged at 450 °C, and b) HPT KD aged at 500 °C, where Fe atoms (pink) and 35 at.% Cr iso-surface (blue) are displayed; c) statistical proxigrams based on 35 at.% Cr iso-surface from HPT KD aged at 450 °C for 500h.

The HPT processed alloys tend to be thermally unstable, owing to NC grain size and high dislocation densities. Consequently, it is important to investigate the stability of the microstructure of HPT KD during aging at 450 and 500 °C. Figure 7a and 7b display

BSE-SEM micrographs; the average grain size of HPT KD aged at 450 °C and 500 °C for 500 h was estimated to be 384 \pm 226 nm, and 518 \pm 123 nm, respectively. The average grain size was determined from 200 grains (excluding grains in the edges) with the ~72% grains falling within one standard deviation denoted by ' \pm '. This result suggests that HPT KD has undergone grain growth as the average grain size of unaged HPT KD is 75 \pm 40 nm [20]. HPT KD grain size increased after aging owing to the high fraction of high angle grain boundaries (misorientation > 20°) which are expected to provide the driving force during aging to undergo grain growth [32]. Grain growth during aging contributes to softening through the Hall-Petch relationship. Larger grains and no α ′ precipitation in the 500 °C aged HPT sample contributes to its lower hardness compared to the same sample aged at 450 °C or the 500 °C aged CG sample.

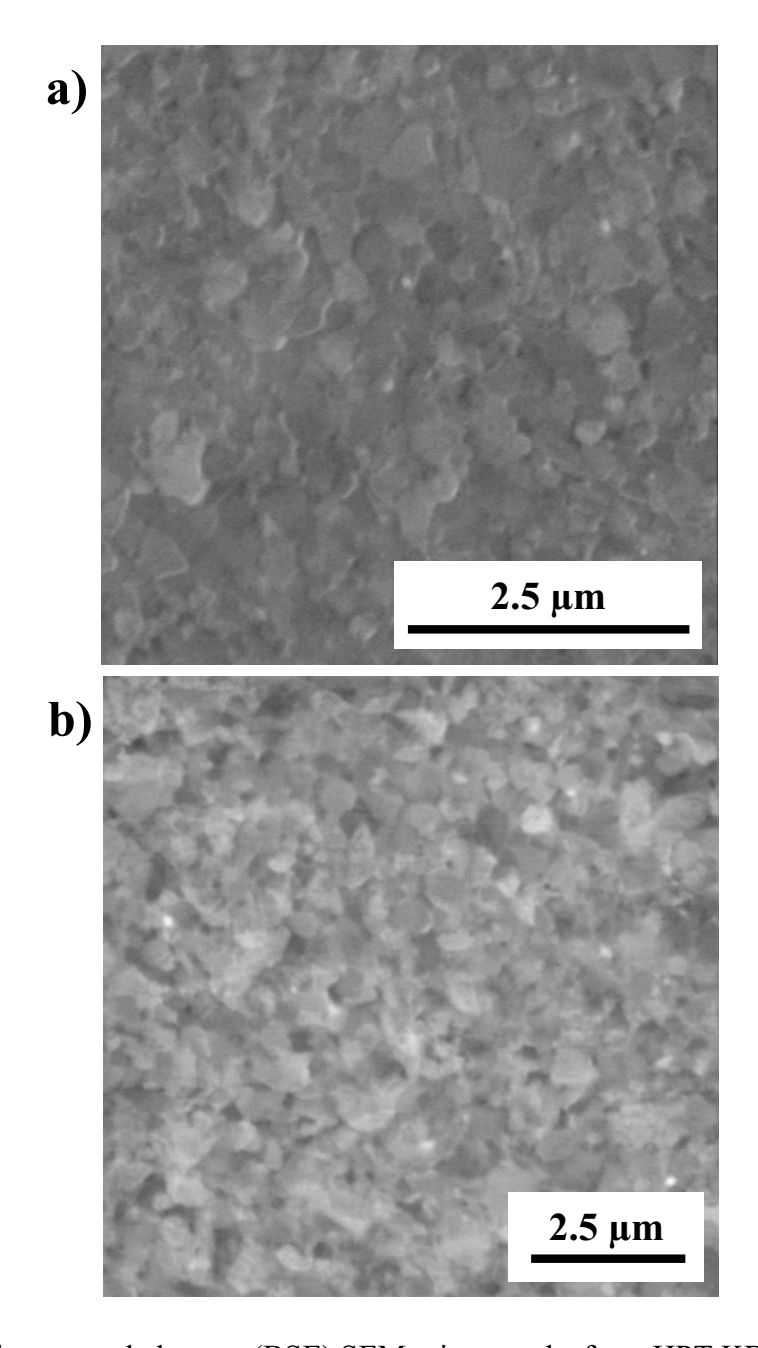


Figure 7. Back scattered electron (BSE) SEM micrographs from HPT KD aged at a) 450 $^{\rm o}$ C, and b) 500 $^{\rm o}$ C.

4. DISCUSSION

Although this study does not involve varying the duration of aging, there are studies that investigated the evolution of α' Cr as a function of aging time[12,16,22,33,34]. APT results from aged PM 2000 ODS FeCrAl obtained by Capdevila et. al show that Cr concentration in the α' phase increased with increasing aging time [34,35]. Therefore, the separation of α' from the Fe-rich α matrix cannot simply be categorized either as spinodal decomposition, or classic nucleation and growth. Jarmila et. al used complimentary non-destructive techniques of magnetic Barkhausen noise, positron annihilation spectroscopy and Mössbauer spectroscopy to study the phase separation of Cr-rich α' from the Fe-rich ferritic α phase in PM2000 aged at 475 °C [15]. Positron annihilation spectroscopy was exclusively utilized to establish a relationship between vacancy concentration and Cr precipitation. They reported that Cr-rich zones could be traced to the path of diffusion of the vacancy clusters and vacancy agglomerations. This suggests that the appearance of α ' in FeCrAl alloys is affected by the thermal vacancy concentration regardless of the process, i.e. spinodal decomposition or classic nucleation and growth. Therefore, the difference in thermal vacancy concentrations caused by varying temperature, grain size, and strain imparted from SPD will have to be taken into consideration to explain the differences in the age hardening behavior of CG, ECAP, and HPT KD.

4.1. Influence of deformation-induced defects on the precipitation behavior in aged ECAP KD

CG KD exhibited a higher degree of age hardening compared to ECAP KD. The hardness of CG KD further increased after aging at 500 °C as compared to that after aging at 450 °C, whereas ECAP KD aged at 500 °C exhibited hardening very similar to that at 450 °C. It has been established from EBSD that ECAP KD is thermally stable during aging at 450 °C and 500 °C. Therefore, the hardening in both CG and ECAP KD is dominated by the precipitation of α'. Considering the size and morphology of α', the Orowan looping mechanism [36] may be utilized to semi-quantitatively explain the differences in the degree of hardening in CG and ECAP KD. Precipitate hardening based on Orowan looping mechanism is given by Equation 1,

$$\Delta \sigma_{or} = M \frac{0.4Gb}{\pi \lambda} \frac{\ln (2\bar{r}/b)}{\sqrt{1-\nu}} \tag{1}$$

where M is the mean orientation factor for polycrystalline body-centered cubic (BCC) materials, G is the shear modulus of the matrix, $b = \sqrt{3}/2 a$ is the Burgers vector magnitude (a is the lattice parameter), \bar{r} is the mean radius of circular cross-section of the spherical precipitate, v is the Poisson's ratio, and λ is the inter-precipitate spacing, given by Equation 2,

$$\lambda = 2\bar{r}\sqrt{\frac{\pi}{4f} - 1} \tag{2}$$

where *f* is the volume fraction of precipitates in the BCC matrix.

From Equations 1 and 2, the larger the average radius is (or the lower the number density of the precipitates is), the larger the inter-precipitate spacing is, and accordingly the lower the degree of hardening is.

Since there is a Cr concentration gradient across neighbouring α' , isoconcentration surfaces appear to be connected between the α ' appearing to be spinodal decomposition [33,35]. However, α ' can be isolated using cluster analysis [37–39]. Cluster analysis within the APT data based on the maximum separation algorithm using IVAS 3.8.4 was utilized to determine the size and number density of α' precipitates in CG and ECAP KD aged at 450 and 500 °C. Clusters of solute atoms are identified by the distance between atoms being smaller than a critical "maximum separation" distance, d_{max}. Cluster count and size distribution analysis was performed to determine d_{max}, and a threshold for the number of additional solute atoms with d_{max} for potential clusters (order parameter in IVAS), as well as the minimum number of solute atoms (N_{min}). These three parameters were set to 0.50, 1 and 40, respectively. L, spacing threshold for the envelope algorithm to add other ranged ion types, as well as D_{erosion} to erode a shell of atoms from the cluster perimeter to account for the shell excess added by the envelope algorithm, were both set to 0.5. In order to avoid variation coming from local inhomogeneity in the α' phase separation behavior with an APT reconstruction, the entire analysis volume was used for cluster analysis.

Results from the cluster analysis, specifically radius and number density of α' precipitates, are displayed in Tables 2 and 3. For the sake of comparison, precipitate characteristics are presented separately for the different aging temperatures of 450 and 500 °C.

Table 2. Cluster analysis values obtained from the APT data representing the precipitate characteristics in CG and ECAP KD aged at 450 °C for 500h.

Sample	CG Kanthal-D	450 °C 500 h	ECAP Kanthal-D 450 °C 500 h		
APT analysis volume	Volume 1	Volume 2	Volume 1	Volume 2	
Average radius (nm)	2.81	2.76	4.21	4.17	
Number density (x 10 ²³ /m ³	7.17	7.45	4.78	5.11	

Table 3. Cluster analysis values obtained from the APT data representing the precipitate characteristics in CG and ECAP aged at 500 °C for 500h.

Sample	CG Kanthal-D	500 °C 500 h	ECAP Kanthal-D 500 °C 500 h		
APT analysis volume	Volume 1	Volume 2	Volume 1	Volume 2	
Average radius (nm)	3.12	3.19	4.61	4.54	
Number density (x 10 ²³ /m ³	8.21	8.60	4.29	4.34	

For both aging temperatures of 450 and 500 °C, the α'precipitate radius is larger while the number density of precipitates is lower in aged ECAP KD compared to those in aged CG KD. This explains the lower degree of hardening of ~75 HV in ECAP KD as opposed to ~105 HV in CG KD, assuming that the precipitate hardening follows the Orowan looping mechanism. In the case of 500 °C aging, an increase in the precipitate radius was found in CG KD along with an increase in the number density. This observation elucidates the reason for CG KD aged at 500 °C to have a further increase in hardness of ~47 HV than that at 450 °C. In contrast, ECAP KD aged at 500 °C shows precipitate characteristics very similar to those at 450 °C, which explains the similar hardness of ECAP KD after aging at 500 °C and 450 °C.

It is well known that a significant density of lattice defects is introduced in metals during SPD [20,40,41]. Čížek et al. reported that the concentration of deformation-induced vacancies introduced by SPD approaches that at the melting point of the material [42]. They also found that, although a majority of the vacancy clusters get annihilated at GBs after diffusion, the remaining vacancy clusters agglomerate and remain in the SPD produced UFG materials. In addition, Al has been shown to stabilize vacancies in Fe-Al alloys by Herrmann et. al [18]. Since KD has 4.7 wt.% Al, it is expected that Al stabilizes the deformation-induced vacancies from SPD in ECAP KD. These vacancies or vacancy clusters facilitate precipitation once they become mobile when activated by elevated temperature [43,44].

In addition, a notable density of dislocations and a significant volume fraction of GBs are created during ECAP. Dislocations and GBs are both "short-circuits" for diffusion (pipe diffusion), significantly increasing diffusion rates and accordingly enhancing precipitation kinetics, which finally leads to coarsening of precipitates (i.e., resulting in larger precipitate sizes and a lower number density of precipitates) [45]. The precipitation behavior in ECAP KD is consistent with that in an earlier study conducted by Read and Murakami, where extruded and rolled MA956 showed coarser α' precipitates in comparison to those in the recrystallized material [21]. Furthermore, in the ECAP KD, due to enhanced diffusion and therefore faster precipitation kinetics, the precipitation at 450 °C is already near equilibrium, and an increase in the temperature by 50 °C does not really change the precipitate characteristics.

4.2. Sweeping grain boundaries as effective vacancy sinks in HPT KD, hindering precipitation and lowering the miscibility gap

While the CG and ECAP KD grain structures were thermally stable at both 450 and 500 °C, HPT KD underwent grain growth that increased with increasing aging temperature. This means that, during the aging process, the GBs are mobile. To understand the interesting precipitation behavior in HPT KD, the interactions between mobile GBs and vacancies need to be understood.

In general, absorption of vacancies by stationary GBs can lead to dislocation climb and sometimes the displacement of the GBs. However, moving GBs can sweep out a larger number of vacancies as compared to stationary GBs, thereby making them more efficient vacancy sinks [46,47]. Mobile GBs can also act as vacancy sources if the matrix concentration of vacancies is lower than that at equilibrium [19]. A recent modelling study published by McFadden et. al investigated the influence of GB motion on local vacancy concentration based on the sharp interface model of creep deformation in crystalline solids [48]. They reported that the absorption of over-saturated vacancies and/or generation of new vacancies into the grains (if their concentration is below equilibrium) is accelerated by the motion of GBs. If there is a gradient in the vacancy concentration across the GB, GB motion is driven into the grain with the higher vacancy concentration. Simultaneously, the GB motion decreases the concentration gradient across the GB, also reducing the driving force for its migration. The vacancy gradient across the GB is also influenced by the vacancy generation/absorption process.

The very small grain size and ~80% of high-angle GBs (HAGBs, misorientation > 15°) and accordingly high GB energy in NC HPT KD drives grain growth [49]. The grain growth speed is dependent on the annealing temperature owing to more rapid diffusion at

higher temperatures. During grain growth, the directional migration of GBs towards higher vacancy concentration not only consumes the thermal vacancies, but also the SPD-induced defects that would contribute to phase separation of α' [50]. This behavior is anticipated to retard α' phase separation and promote the retention of Cr in the matrix, thereby bringing down the miscibility gap of α - α' .

Phase equilibrium modelling using Thermo-Calc was performed to generate Fe-Cr-Al ternary phase diagram in order to obtain an estimate of the α - α 'miscibility gap. Isothermal sections at 450 and 500 °C are presented in Figure 8. It can be seen that Fe-21Cr-5Al is within the α + α 'dual phase region at 450 °C. In contrast, Fe-21Cr-5Al is present at the edge of the miscibility gap at 500 °C. The GBs in HPT KD are mobile at both 450 and 500 °C, and the miscibility gap is pushed down at both temperatures. At 500 °C, the miscibility gap is lowered to the extent where Fe-21Cr-5Al is pushed into the α -Fe region. In contrast, at 450 °C, despite the lowering of the miscibility gap, Fe-21Cr-5Al is still within the dual phase α + α ' region. These are the reasons why α 'precipitation is observed in HPT KD after 450 °C aging but not after 500 °C aging.

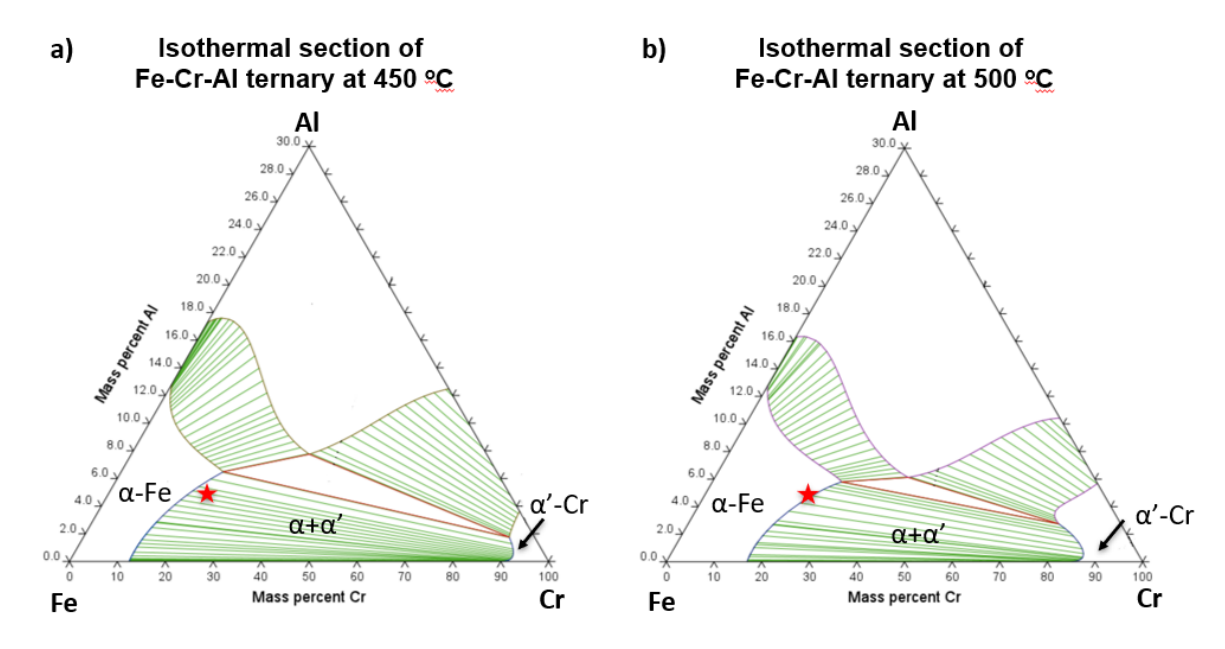


Figure 8. Isothermal section of Fe-Cr-Al ternary phase diagram at a) 450 $^{\circ}$ C, and b) 500 $^{\circ}$ C.

In order to validate the modelling results, aging of CG and ECAP KD was performed at 550 °C to confirm whether or not the miscibility gap is above 500 °C. The hardness after aging at 550 °C was measured to be very similar to that of the unaged counterpart, as shown in Figure 9. This implies that very likely no α' precipitation occurred during aging at 550 °C. Considering that α' precipitation takes place at 500 °C but not at 550 °C, the miscibility gap is between 500 and 550 °C for CG and ECAP KD. In the case of HPT KD, there is α' precipitation during aging at 450 °C but not at 500 °C; thus, the miscibility gap is between 450 and 500 °C for the HPT sample. Again, the α - α' miscibility gap is lowered in HPT KD as compared to that in CG and ECAP KD due to the high density of GBs and GB motion during aging. Hence, it is clear that there is a direct correlation between grain size and α' phase separation in high-Cr ferritic FeCrAl alloys.

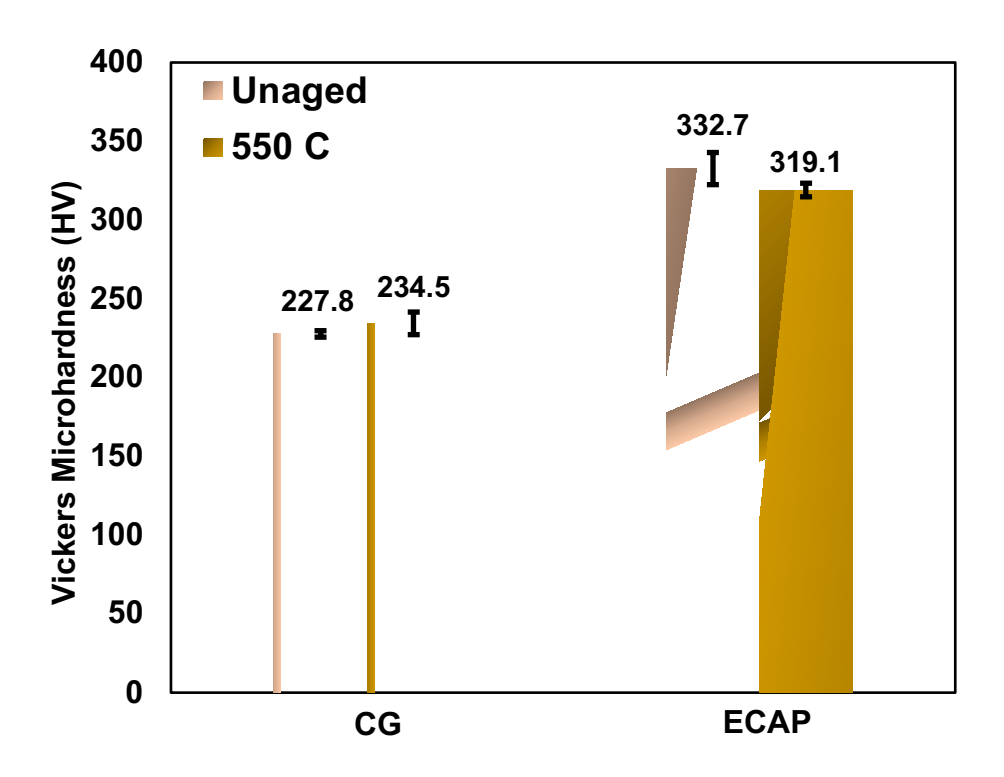


Figure 9. Average Vickers microhardness obtained from CG and ECAP KD that were unaged or aged at 550 °C.

4.3. MD simulation to understand influence of grain size on concentration of vacancies

Molecular dynamics (MD) simulations were carried out to investigate the stability of vacancies in the matrix of grains and GBs. A bicrystal model was created to form $\Sigma 3$ GBs that are commonly observed by experiments [51], and the method was well described in [52]. The total number of atoms is about 6 million, and periodic boundary conditions are applied to all three directions. The initial system contains 70 at.% Fe, 20 at.% Cr, and 10 at.% Al atoms, and they are randomly distributed. An embedded atom method Finnis-Sinclair (EAM-FS) potential derived by Liu et al [53] is used to describe the alloy, and this potential is capable of predicting the mechanical properties and phase

stability for FeCrAl structure [54]. All atomistic simulations were implemented in the LAMMPS software package [55]. Images of atomistic configurations were produced in OVITO [56].

Vacancies were introduced in two different ways: vacancy concentrations range from 10^{-4} to 10^{-2} at.% and the corresponding vacancies were randomly removed in the matrix or in the GBs. We compared the energetics between these two systems containing n vacancies by calculating $\Delta E = (E^{\rm GB} - E^{\rm M})/n$, where $E^{\rm GB}$ and $E^{\rm M}$ are the potential energy for systems contain vacancies in the GBs and the matrix, respectively. Molecular statics (MS) simulations, i.e., energy minimization at T = 0 K, are performed using a conjugate gradient algorithm, imposing zero pressure on the simulation boxes to obtain the stable structure. As shown in Figure 10 (a), the values of ΔE is always negative, which suggests that vacancies are energetically more favorable to stay in the GBs compared to that in the matrix. Figure 10 (b-d) illustrates atomistic configurations of bicrystal model and the distribution of vacancies in two different systems. This MD prediction can support the current experimental observation that less α' precipitation is due to higher density of GBs in NC samples that cause less vacancies in the matrix.

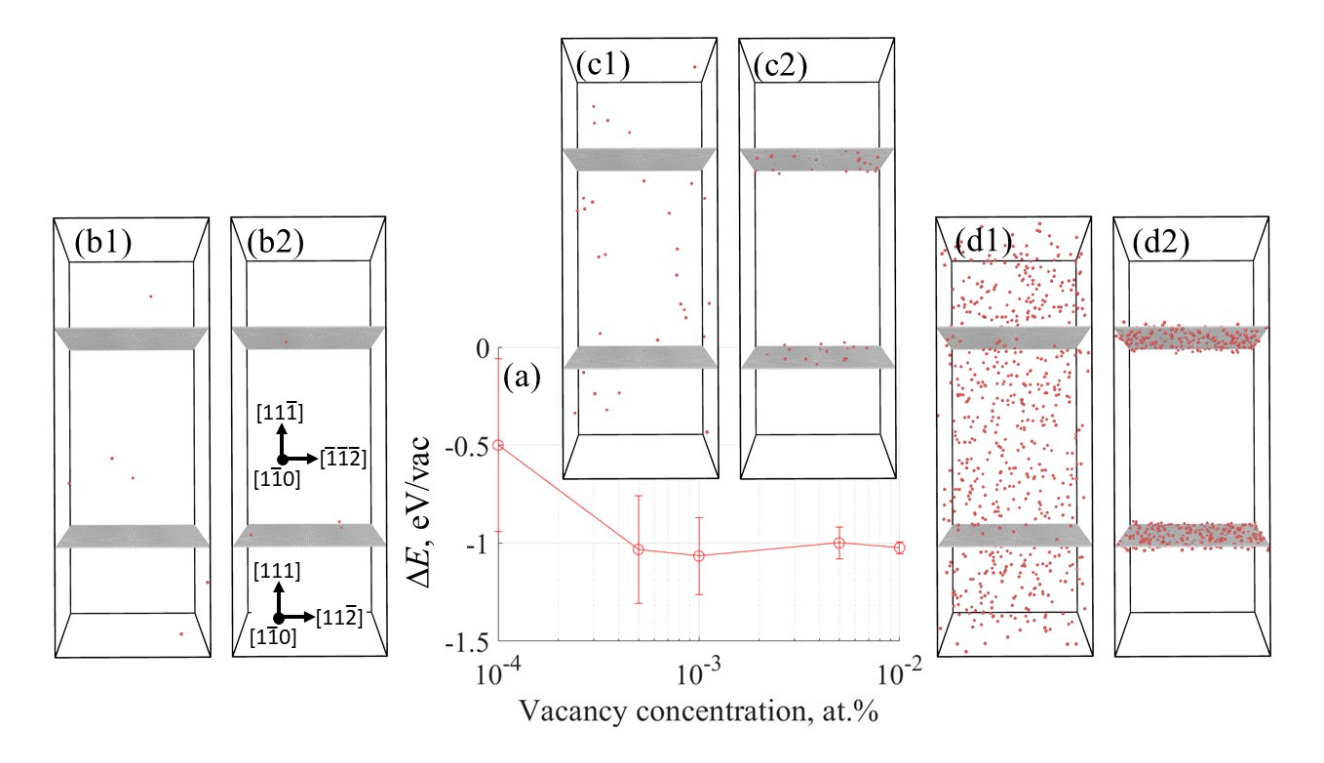


Figure 10. Energy difference as a function of vacancy concentration (a). Vacancy concentration is 10^{-4} at.% for vacancies in the matrix (b1) and GBs (b2); vacancy concentration is 10^{-3} at.% for vacancies in the matrix (c1) and GBs (c2); vacancy concentration is 10^{-2} at.% for vacancies in the matrix (d1) and GBs (d2). GBs are represented by grey atoms, and vacancies are located at positions of red atoms.

5. CONCLUSIONS

Coarse grained (CG), equal-channel angular pressed (ECAP) fine-grained and ultrafine-grained, and high-pressure torsion (HPT) processed nanocrystalline, high-Cr ferritic Kanthal-D [KD; Fe-21Cr-5Al-0.026C (all in wt.%)] were aged at 450, 500 and 550 °C for 500h to understand the influence of grain size on Cr-enriched α' precipitation.

i) Vickers microhardness testing showed that CG KD underwent a higher degree of hardening after aging at 450 and 500 °C as compared to ECAP KD. There was a further increase in hardness observed in CG KD after aging at 500 °C, whereas ECAP KD aged at 500 °C showed similar hardening to that at 450 °C. CG and

- ECAP KD exhibited no hardening after 550 °C aging. HPT KD showed softening after aging, with the degree of softening increasing with an increase in the aging temperature.
- ii) Atom probe tomography (APT) investigations revealed the precipitation of α 'in CG and ECAP KD aged at 450 and 500 °C. Electron backscatter diffraction study confirmed that grain size in ECAP KD was thermally stable at 450 and 500 °C, therefore affirming that the hardening was dominated by α ' precipitation.
- ECAP KD compared to that in aged CG KD. In addition, the precipitation in ECAP KD attained equilibrium/saturation after aging at 450 °C, and an increase in the temperature to 500 °C did not affect the precipitate characteristics. In contrast, CG KD showed a coarser precipitate microstructure with an increase in aging temperature from 450 to 500 °C. These observed differences in precipitation behavior between CG and ECAP KD were attributed to the smaller grain sizes and increased defect (vacancy and dislocation) density in ECAP KD compared to CG KD, enhancing diffusion and precipitation kinetics, which leads to earlier precipitate nucleation and faster coarsening.
- iv) HPT KD underwent grain growth at 450 and 500 °C aging, which softened the alloy due to the Hall-Petch relationship. APT investigations revealed α' precipitation in HPT KD aged at 450 °C but not at 500 °C. The lack of precipitation and larger grain size of the 500 °C aged sample made it softer than the 450 °C aged sample.

v) During the aging of nanocrystalline HPT KD at 450 and 500 °C, the mobile grain boundaries consume vacancies that would facilitate α' precipitation (including thermal vacancies and vacancies created by severe plastic deformation). This inhibits α'precipitation and increases the Cr solubility in the Fe-rich α matrix, lowering the miscibility gap for phase separation. The miscibility gap in HPT KD was reduced to between 450 and 500 °C, compared to between 500 and 550 °C for CG and ECAP KD.

Overall, this work shows that there is a significant influence of grain size on α' precipitation in high-Cr FeCrAl alloys, and grain size needs to be taken into consideration when designing new alloys for industrial applications.

ACKNOWLEDGEMENTS

This research was financially supported by U.S. Department of Energy, Office of Nuclear Energy through the NEET-NSUF (Nuclear Energy Enabling Technology – Nuclear Science User Facility) program (award number DE-NE0008524). Partial support for H. Wen came from the U.S. National Science Foundation (award number DMR-2207965).

R. Islamgaliev is grateful to the Russian Science Foundation in the framework of the Project No. 22-23-00714. R.Z. Valiev acknowledges the support in part by the Ministry of Science and Higher Education of Russian Federation (Agreement No. 075-15-2022-1114 as of 06/30/2022). APT research was supported by the Center for Nanophase Materials Sciences (CNMS), which is a US Department of Energy, Office of Science User Facility at Oak Ridge National Laboratory. The authors would like to thank James

Burns for his assistance in performing APT sample preparation and running the APT experiments. The MD simulation was funded by Atomic Energy of Canada Limited, under the auspices of the Federal Nuclear Science and Technology Program.

Computational resources for the MD simulation work described in this paper were supported by the High-Performance Computing Cluster at Canadian Nuclear Laboratories.

REFERENCES

- [1] Fourth Annual Report High-Temperature Materials and Reactor Component Development Programs, Cincinnati, Ohio, 1965.
- [2] J.F. Collins, F.C. Robertshaw, Advanced Long-Life Reactor Fuel Cladding and Structural Materials Development, Cincinnati, Ohio, 1967. https://www.osti.gov/biblio/4461970.
- [3] G.R. VanHouten, M.R. Broz, Advanced Long-Life Reactor Fuel Element,
 Moderator, Control, and Shield Materials Development, Cincinnati, Ohio, n.d.
- [4] Fifth annual report on high temperature materials programs Part A, 1966.
- [5] Seventh annual report AEC Fuels and Materials Development program, General Electric, 1968.
- [6] High-Temperature Materials Program Progress Report No. 59, Part A, GEMP-59A, 1966.
- [7] High-Temperature Materials Program Progress Report No. 55, Part A, GEMP-55A, 1966.

- [8] G. Bonny, D. Terentyev, L. Malerba, On the α-α' miscibility gap of Fe-Cr alloys, Scr Mater 59 (2008) 1193–1196. https://doi.org/10.1016/j.scriptamat.2008.08.008.
- [9] D. Bhattacharyya, T. Yamamoto, P. Wells, E. Marquis, M. Bachhav, Y. Wu, J. Davis, A. Xu, G.R. Odette, Microstructural changes and their effect on hardening in neutron irradiated Fe-Cr alloys, Journal of Nuclear Materials 519 (2019) 274–286. https://doi.org/10.1016/j.jnucmat.2019.03.022.
- [10] S.A. Briggs, P.D. Edmondson, K.C. Littrell, Y. Yamamoto, R.H. Howard, C.R. Daily, K.A. Terrani, K. Sridharan, K.G. Field, A combined APT and SANS investigation of α' phase precipitation in neutron-irradiated model FeCrAl alloys, Acta Mater 129 (2017) 217–228. https://doi.org/10.1016/j.actamat.2017.02.077.
- [11] C. Capdevila, M.K. Miller, J. Chao, Phase separation kinetics in a Fe-Cr-Al alloy, Acta Mater 60 (2012) 4673–4684. https://doi.org/10.1016/j.actamat.2012.05.022.
- [12] S. Kobayashi, T. Takasugi, Mapping of 475 °c embrittlement in ferritic Fe-Cr-Al alloys, Scr Mater 63 (2010) 1104–1107.

 https://doi.org/10.1016/j.scriptamat.2010.08.015.
- [13] W. Han, K. Yabuuchi, A. Kimura, S. Ukai, N. Oono, T. Kaito, T. Torimaru, S. Hayashi, Effect of Cr/Al contents on the 475°C age-hardening in oxide dispersion strengthened ferritic steels, Nuclear Materials and Energy 9 (2016) 610–615. https://doi.org/10.1016/j.nme.2016.05.015.
- [14] Z. Yang, Z.X. Wang, C.H. Xia, M.H. Ouyang, J.C. Peng, H.W. Zhang, X.S. Xiao, Aluminum suppression of α' precipitate in model Fe–Cr–Al alloys during long-term aging at 475 °C, Materials Science and Engineering A 772 (2020) 138714. https://doi.org/10.1016/j.msea.2019.138714.

- [15] J. Degmová, V. Kršjak, S. Sojak, J. Dekan, M. Petriska, P. Mikula, M. Kotvas, NDT study of precipitation processes in thermally aged Fe-20Cr alloy, Journal of Nuclear Materials 547 (2021). https://doi.org/10.1016/j.jnucmat.2021.152799.
- [16] C. Capdevila, M.K. Miller, K.F. Russell, Aluminum partitioning during phase separation in Fe-20%Cr-6%Al ODS alloy, J Mater Sci 43 (2008) 3889–3893. https://doi.org/10.1007/s10853-007-2228-z.
- [17] H.G. Read, H. Murakami, K. Hono, Al partitioning in MA 956, an ods ferritic stainless steel, Scr Mater 36 (1997) 355–361. https://doi.org/10.1016/S1359-6462(96)00388-0.
- [18] J. Herrmann, G. Inden, G. Sauthoff, Deformation behaviour of iron-rich iron-aluminum alloys at low temperatures, Acta Mater 51 (2003) 2847–2857. https://doi.org/10.1016/S1359-6454(03)00089-2.
- [19] Y. Mishin, G.B. McFadden, R.F. Sekerka, W.J. Boettinger, Sharp interface model of creep deformation in crystalline solids, Phys Rev B Condens Matter Mater Phys 92 (2015). https://doi.org/10.1103/PhysRevB.92.064113.
- [20] M. Arivu, A. Hoffman, J. Duan, H. Wen, R. Islamgaliev, R. Valiev, Severe plastic deformation assisted carbide precipitation in Fe-21Cr-5Al alloy, Mater Lett 253 (2019) 78–81. https://doi.org/10.1016/j.matlet.2019.05.139.
- [21] H.G. Read, H. Murakami, Microstructural influences on the decomposition of an Al-containing ferritic stainless steel, Appl Surf Sci 94–95 (1996) 334–342. https://doi.org/10.1016/0169-4332(95)00524-2.
- [22] C. Capdevila, M.M. Aranda, R. Rementeria, R. Domínguez-Reyes, E. Urones-Garrote, M.K. Miller, Influence of nanovoids on α-α' Phase separation in FeCrAl

- oxide dispersion strengthened alloy, Scr Mater 110 (2016) 53–56. https://doi.org/10.1016/j.scriptamat.2015.07.044.
- [23] F. Djavanroodi, M. Ebrahimi, B. Rajabifar, S. Akramizadeh, Fatigue design factors for ECAPed materials, Materials Science and Engineering A 528 (2010) 745–750. https://doi.org/10.1016/j.msea.2010.09.080.
- [24] A.P. Zhilyaev, T.G. Langdon, Using high-pressure torsion for metal processing: Fundamentals and applications, Prog Mater Sci 53 (2008) 893–979. https://doi.org/10.1016/j.pmatsci.2008.03.002.
- [25] K. Thompson, D. Lawrence, D.J. Larson, J.D. Olson, T.F. Kelly, B. Gorman, In situ site-specific specimen preparation for atom probe tomography, Ultramicroscopy 107 (2007) 131–139. https://doi.org/10.1016/j.ultramic.2006.06.008.
- [26] O.C. Hellman, J.A. Vandenbroucke, J. Rüsing, D. Isheim, D.N. Seidman, Analysis of Three-dimensional Atom-probe Data by the Proximity Histogram, Microscopy and Microanalysis 6 (2000) 437–444. https://doi.org/10.1007/S100050010051.
- [27] T.L. Martin, A. Radecka, L. Sun, T. Simm, D. Dye, K. Perkins, B. Gault, M.P. Moody, P.A.J. Bagot, Insights into microstructural interfaces in aerospace alloys characterised by atom probe tomography, Materials Science and Technology (United Kingdom) 32 (2016) 232–241.
 https://doi.org/10.1179/1743284715Y.0000000132.
- [28] K.E. Yoon, R.D. Noebe, O.C. Hellman, D.N. Seidman, Dependence of interfacial excess on the threshold value of the isoconcentration surface, in: Surface and

- Interface Analysis, John Wiley and Sons Ltd, 2004: pp. 594–597. https://doi.org/10.1002/sia.1708.
- [29] O.C. Hellman, D.N. Seidman, Measurement of the Gibbsian interfacial excess of solute at an interface of arbitrary geometry using three-dimensional atom probe microscopy, 2002. www.elsevier.com/locate/msea.
- [30] H. Wen, T.D. Topping, D. Isheim, D.N. Seidman, E.J. Lavernia, Strengthening mechanisms in a high-strength bulk nanostructured Cu-Zn-Al alloy processed via cryomilling and spark plasma sintering, Acta Mater 61 (2013) 2769–2782. https://doi.org/10.1016/j.actamat.2012.09.036.
- [31] C. Du, S. Jin, Y. Fang, J. Li, S. Hu, T. Yang, Y. Zhang, J. Huang, G. Sha, Y. Wang, Z. Shang, X. Zhang, B. Sun, S. Xin, T. Shen, Ultrastrong nanocrystalline steel with exceptional thermal stability and radiation tolerance, Nat Commun 9 (2018) 1–9. https://doi.org/10.1038/s41467-018-07712-x.
- [32] M. Arivu, A. Hoffman, J. Duan, J. Poplawsky, X. Zhang, F. Liou, R. Islamgaliev, R. Valiev, H. Wen, Comparison of the Thermal Stability in Equal-Channel-Angular-Pressed and High-Pressure-Torsion-Processed Fe–21Cr–5Al Alloy, Adv Eng Mater (2023). https://doi.org/10.1002/adem.202300756.
- [33] C. Capdevila, M.K. Miller, G. Pimentel, J. Chao, Influence of recrystallization on phase separation kinetics of oxide dispersion strengthened Fe Cr Al alloy, Scr Mater 66 (2012) 254–257. https://doi.org/10.1016/j.scriptamat.2011.11.003.
- [34] C. Capdevila, M.K. Miller, K.F. Russell, J. Chao, J.L. González-Carrasco, Phase separation in PM 2000TM Fe-base ODS alloy: Experimental study at the atomic

- level, Materials Science and Engineering: A 490 (2008) 277–288. https://doi.org/10.1016/j.msea.2008.01.029.
- [35] C. Capdevila, M.K. Miller, J. Chao, Phase separation kinetics in a Fe-Cr-Al alloy, Acta Mater 60 (2012) 4673–4684. https://doi.org/10.1016/j.actamat.2012.05.022.
- [36] H. Wen, T.D. Topping, D. Isheim, D.N. Seidman, E.J. Lavernia, Strengthening mechanisms in a high-strength bulk nanostructured Cu-Zn-Al alloy processed via cryomilling and spark plasma sintering, Acta Mater 61 (2013) 2769–2782. https://doi.org/10.1016/j.actamat.2012.09.036.
- [37] L.T. Stephenson, M.P. Moody, P. V. Liddicoat, S.P. Ringer, New Techniques for the Analysis of Fine-Scaled Clustering Phenomena within Atom Probe Tomography (APT) Data, Microscopy and Microanalysis 13 (2007) 448–463. https://doi.org/10.1017/S1431927607070900.
- [38] E.A. Marquis, J.M. Hyde, Applications of atom-probe tomography to the characterisation of solute behaviours, Materials Science and Engineering: R: Reports 69 (2010) 37–62. https://doi.org/10.1016/j.mser.2010.05.001.
- [39] B. Gault, A. Chiaramonti, O. Cojocaru-Mirédin, P. Stender, R. Dubosq, C. Freysoldt, S.K. Makineni, T. Li, M. Moody, J.M. Cairney, Atom probe tomography, Nature Reviews Methods Primers 1 (2021) 51. https://doi.org/10.1038/s43586-021-00047-w.
- [40] W. Lechner, W. Puff, B. Mingler, M.J. Zehetbauer, R. Würschum, Microstructure and vacancy-type defects in high-pressure torsion deformed Al-Cu-Mg-Mn alloy, Scr Mater 61 (2009) 383–386. https://doi.org/10.1016/j.scriptamat.2009.04.027.

- [41] D. Setman, E. Schafler, E. Korznikova, M.J. Zehetbauer, The presence and nature of vacancy type defects in nanometals detained by severe plastic deformation, Materials Science and Engineering A 493 (2008) 116–122. https://doi.org/10.1016/j.msea.2007.06.093.
- [42] J. Čížek, M. Janeček, T. Vlasák, B. Smola, O. Melikhova, R.K. Islamgaliev, S. v. Dobatkin, The development of vacancies during severe plastic deformation, Mater Trans 60 (2019) 1533–1542. https://doi.org/10.2320/matertrans.MF201937.
- [43] A. Hoffman, H. Wen, R. Islamgaliev, R. Valiev, High-pressure torsion assisted segregation and precipitation in a Fe-18Cr-8Ni austenitic stainless steel, Mater Lett 243 (2019) 116–119. https://doi.org/10.1016/j.matlet.2019.02.030.
- [44] A. Hoffman, M. Arivu, H. Wen, L. He, K. Sridharan, X. Wang, W. Xiong, X. Liu, L. He, Y. Wu, Enhanced Resistance to Irradiation Induced Ferritic Transformation in Nanostructured Austenitic Steels, Materialia (Oxf) 13 (2020) 100806. https://doi.org/10.1016/j.mtla.2020.100806.
- [45] I. Chesser, R.K. Koju, Y. Mishin, Atomic-level mechanisms of short-circuit diffusion in materials, International Journal of Materials Research 115 (2024) 85– 105. https://doi.org/10.1515/ijmr-2023-0202.
- [46] J. Svoboda, F.D. Fischer, P. Fratzl, Diffusion and creep in multi-component alloys with non-ideal sources and sinks for vacancies, Acta Mater 54 (2006) 3043–3053. https://doi.org/10.1016/j.actamat.2006.02.041.
- [47] J. Svoboda, F.D. Fischer, Modelling of the influence of the vacancy source and sink activity and the stress state on diffusion in crystalline solids, Acta Mater 59 (2011) 1212–1219. https://doi.org/10.1016/j.actamat.2010.10.054.

- [48] G.B. McFadden, W.J. Boettinger, Y. Mishin, Effect of vacancy creation and annihilation on grain boundary motion, Acta Mater 185 (2020) 66–79. https://doi.org/10.1016/j.actamat.2019.11.044.
- [49] J. Duan, H. Wen, C. Zhou, X. He, R. Islamgaliev, R. Valiev, Annealing behavior in a high-pressure torsion-processed Fe–9Cr steel, J Mater Sci 55 (2020) 7958–7968. https://doi.org/10.1007/s10853-020-04560-3.
- [50] M. Winning, A.D. Rollett, G. Gottstein, D.J. Srolovitz, A. Lim, L.S. Shvindlerman, Mobility of low-angle grain boundaries in pure metals, Philosophical Magazine 90 (2010) 3107–3128.
 https://doi.org/10.1080/14786435.2010.481272.
- [51] H. Beladi, G.S. Rohrer, The relative grain boundary area and energy distributions in a ferritic steel determined from three-dimensional electron backscatter diffraction maps, Acta Mater 61 (2013) 1404–1412.

 https://doi.org/https://doi.org/10.1016/j.actamat.2012.11.017.
- [52] C. Dai, N. Ofori-Opoku, A. Prudil, M. Welland, Atomistic modeling of Σ3 twin grain boundary in alloy 800H, Comput Mater Sci 212 (2022) 111573.
 https://doi.org/10.1016/j.commatsci.2022.111573.
- [53] Z. Liu, Q. Han, Y. Guo, J. Lang, D. Shi, Y. Zhang, Q. Huang, H. Deng, F. Gao, B. Sun, S. Du, Development of interatomic potentials for Fe-Cr-Al alloy with the particle swarm optimization method, J Alloys Compd 780 (2019) 881–887. https://doi.org/https://doi.org/10.1016/j.jallcom.2018.11.079.
- [54] H. Yao, T. Ye, W. Yu, P. Wang, J. Wu, Y. Wu, P. Chen, Atomic-scale investigation of creep behavior and deformation mechanism in nanocrystalline

- FeCrAl alloys, Mater Des 206 (2021) 109766. https://doi.org/https://doi.org/10.1016/j.matdes.2021.109766.
- [55] A.P. Thompson, H.M. Aktulga, R. Berger, D.S. Bolintineanu, W.M. Brown, P.S. Crozier, P.J. in 't Veld, A. Kohlmeyer, S.G. Moore, T.D. Nguyen, R. Shan, M.J. Stevens, J. Tranchida, C. Trott, S.J. Plimpton, LAMMPS a flexible simulation tool for particle-based materials modeling at the atomic, meso, and continuum scales, Comput Phys Commun 271 (2022) 108171.
 https://doi.org/10.1016/j.cpc.2021.108171.
- [56] A. Stukowski, Visualization and analysis of atomistic simulation data with OVITO-the Open Visualization Tool, Model Simul Mat Sci Eng 18 (2010) 15012. https://doi.org/10.1088/0965-0393/18/1/015012.